Sizing and Ranging Criteria for SAR Images of Steel and Wood Specimens

Viet Le, Tzuyang Yu, Jones OwusuTwumasi, and Qixiang Tang

Department of Civil and Environmental Engineering

University of Massachusetts Lowell

One University Avenue, Lowell, MA 01854, U.S.A.

ABSTRACT

The use of microwave and radar sensors in the nondestructive evaluation (NDE) of damaged materials and structures has been proven to be a promising approach. In this paper, a portable imaging radar sensor utilizing 10 GHz central frequency and stripmap synthetic aperture radar (SAR) imaging was applied to steel and wood specimens for size and range determination. Relationships between range and properties of SAR images (e.g. maximum amplitude and total SAR amplitude) were developed and reported for various specimens including a steel bar (2.5 cm by 2.5 cm by 28.5 cm), a wood bar (2.5 cm by 2.5 cm by 28.5 cm), a steel plate (39.7 cm by 57.9 cm by 1.75 cm), and a wood board (30.5 cm by 30.5 cm by 1.8 cm). Various ranges from 30 cm to 100 cm were used on these specimens. In our experiment, attenuation of radar signals collected by the imaging radar system on different material specimens was measured and modeled. Change in the attenuation of maximum SAR amplitude was observed in different materials. It is found that SAR images can be used to distinguish materials of different compositions and sizes.

Keywords: Synthetic aperture radar imaging, microwave frequency, radar NDE, electromagnetic sensing, structural health monitoring

1. INTRODUCTION

The gradual deterioration of the United States' critical civil infrastructure has been no secret to civil engineers and the public. The American Society of Civil Engineers (ASCE) has reported on the severe condition of the nation's bridges, dams, roads, railways, ports and other civil engineering systems.[1–4] By appointing many grades of "C" and "D" to these systems in the 2015 report cards for the infrastructure in several states such as New York, Virginia, Iowa, and Arizona, the critical status of these systems and their increasing risks of failure has been recognized.

To better monitor the degradation of aging civil infrastructure, structural health monitoring (SHM) has arisen as a viable means of providing valuable information. Advancements in this field include development of innovative nondestructive evaluation (NDE) techniques that can communicate knowledge on the condition of a material, component, or system to these professionals. Examples include acoustic methods, thermal methods, and electromagnetic (EM) methods.[5,6] Among these techniques, EM methods represent a new age of rapid, distant, and efficient NDE techniques for civil infrastructures. This has been most prominent in the use of radar and microwave sensors on dielectric or conductive materials.[5] For example, ground-penetrating radar (GPR) utilizes a transmitting antenna that triggers EM pulses in the microwave band.[7,8] The interfaces of materials with varying dielectric properties reflect these waves which are collected by the receiving antenna to produce B-scan or C-scan figures. This information is then used for an assortment of applications in subsurface EM sensing including rebar detection, thickness measurements, or identification of voids and cracks.[9–11] Radar technology is not just limited to GPR. Developments of a wideband subsurface imaging radar for the distant inspection of civil infrastructures have also been recently reported.[11–14] EM sensors utilizing surface EM reflections and synthetic aperture radar (SAR) imaging algorithms have been used in subsurface sensing for detecting damages on a test subject, identifying its material properties, and locating the presence of objects such as steel rebar.[11–14]

Further author information: (Send correspondence to T. Yu)

E-mail: tzuyang_yu@UML.EDU, Telephone: 1 978 934 2288

The objective of this paper is to present our research on the use of a continuous wave imaging radar (CWIR) system for the determination of size and range of targets using steel and wood specimens as examples. In this paper, a background on SAR imaging is first provided. A series of laboratory experiments utilizing stripmap SAR imaging and backprojection algorithms to generate SAR images from radar signals collected in the frequency range of 1 GHz to 18 GHz by a two-dimensional positioning system at UMass Lowell is then presented. Analysis of SAR images is provided. Finally, research findings are summarized.

2. SYNTHETIC APERTURE RADAR

2.1 Background

One of radar's initial limitations was caused by poor resolution due to the size restriction of a longer and more cumbersome physical antenna. Shorter wavelengths could not be used to improve resolution since they would attenuate severely in lossy dielectrics. Synthetic aperture radar (SAR) was developed as a signal processing tool to overcome this issue.[15] The movement of a small radar antenna was used to mimic or "synthesize" a large antenna around a test subject, allowing for the use of longer wavelengths while maintaining an excellent resolution with a smaller, more manageable antenna. During the time that the test subject is within the system's target view, backscattered echoes from transmitted EM waves are recorded and processed for imaging purposes. There are several modes with which SAR can be used: spotlight, stripmap, and inverse. The CWIR system at UMass Lowell utilizes the stripmap SAR mode where the antenna is held in a fixed pointing direction along its path of movement.

2.2 Signal Processing and Image Reconstruction

In the CWIR system at UMass Lowell, SAR and backprojection algorithms are employed to image returned/reflected radar signals.[13, 14, 16] A summary of the primary steps in SAR imaging is described as follows, and the monostatic radar operation where different incident angles (θ_m) and frequencies (ω_n) form a data plane using inverse SAR mode is illustrated in Fig. 1.[13] First, the time-independent SAR point response is defined as:
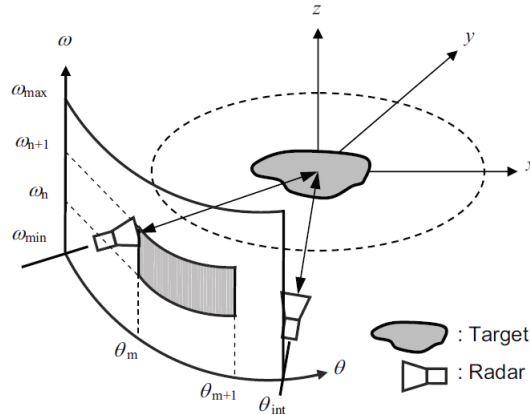

Figure 1. Definition of inspection angle on the image plane.[13]

$$S(x, ysin\theta_i) = \text{sinc}\left(\frac{\pi y sin\theta_i}{\rho_r}\right) \text{sinc}\left(\frac{\pi x}{\rho_{xr}}\right) \tag{1}$$

where (x, y, z) are coordinates on the plane of radar inspection, θ_i is the incident angle with respect to the z axis, ρ_r is the range resolution of the radar (distance from the radar system to the test subject), and ρ_{xr} is the cross-range resolution of the radar (distance of the path of travel of the radar system). $\text{sinc}(x) = \dfrac{sin(x)}{x}$ is the

sinc function. Subsequently, the time-dependent scattering response of a point scatterer $\bar{r}_j$ observed by the radar at $\bar{r}_s$ can then be expressed as follows in terms of time variable t and $\bar{r}_{s,j}$:

$$S(\bar{r}_{s,j}, t) = \frac{1}{r_{s,j}^2} \int_{\omega_c - \pi B}^{\omega_c + \pi B} d\omega \cdot \exp\left[i\omega t\right] \tag{2}$$

$\bar{r}_{s,j}$ is the difference between $\bar{r}_s - \bar{r}_j$ where $\bar{r}_s$ is the radar position vector and $\bar{r}_j$ is the position vector of the jth scatterer. $r_{s,j} = |\bar{r}_{s,j}|$ is the distance between the radar and the jth scatterer, ω_c is the radian center frequency, i is the imaginary number, ω is the radian frequency variable, and B is the frequency bandwidth.

Integration and range compression on $S(\bar{r}_{s,j}, t)$ is conducted by shifting t to $\hat{t} = t - \frac{r_{s,j}}{c}$ where c is the speed of the radar signals. The backprojection processing, expressed by the following equation, is then carried out through integration of all range-compressed focused radar signals to obtain $D(\xi, \hat{t})$, where ξ is the position of the radar traveling on its synthetic aperture.

$$B_{BP}(\xi, t) = C_{BP} \cdot \frac{\partial D(\xi, t)}{\partial t} \tag{3}$$

C_{BP} is the backprojection coefficient defined in order to yield an ideal bandpass transfer function. Lastly, the following equation yields the backprojected SAR image, I:

$$I(\bar{r}, \phi) = \int_0^{\bar{r}_s \theta_{int}} d\xi \cdot B_{BP}(\xi, t) \tag{4}$$

where $(\bar{r}, \phi)$ are the polar coordinates of the SAR image on the range vs. cross-range plane and θ_{int} is the synthetic aperture. SAR imaging algorithms and backprojections have been demonstrated as a powerful tool especially for far-field airborne radar NDE. Its vast capabilities and the theories behind it have been reported in literature.[13, 14, 16]

3. EXPERIMENTAL SETUP

3.1 Continuous Wave Imaging Radar

The CWIR system was built inside a custom-made anechoic chamber constructed for collecting laboratory distant radar responses of specimens as seen in Fig. 2. Electromagnetic absorbing materials were installed on the interior of the chamber to create a reflectionless environment. The configuration allows scans of up to approximately 1.8 m (6 ft) in the cross-range direction and approximately 3 m (10 ft) in the range direction. The radar instrument seen in the right hand side of Fig. 2 was supported by a two-dimensional positioning system. This system can move the radar horizontally or vertically. When radar scans were conducted, the target specimen was placed at a specified range distance R away from the radar on top of a stand that was also covered by EM absorbing materials. The anechoic chamber along with the placement of the EM absorbing materials reduced the interference of EM noises from the background.

The CWIR system emitted EM waves at a central frequency of 10 GHz with bandwidth of 1.5 GHz. The frequency was within the X-band range because of the small size and low cost of the antenna, transmitter, and other components. As mentioned previously, the CWIR system utilizes stripmap SAR imaging algorithm; therefore, the angle at which the radar antenna points at the subject remained the same throughout the scan.

3.2 Specimen and Experimental Setup Description

Steel and wood specimens were selected for this study: a steel bar (2.5 cm by 2.5 cm by 28.5 cm), a wood bar (2.5 cm by 2.5 cm by 28.5 cm), a steel plate (39.7 cm by 57.9 cm by 1.75 cm), and a wood board (30.5 cm by 30.5 cm by 1.8 cm). These specimens are shown in Fig. 3. Each specimen was scanned at six ranges ($R = 30$, 40, 50, 80, 90, and 100 cm). In addition, the wood bar was also scanned by rotating about its vertical axis by $90°$ and $180°$. In total, the entire experiment consisted of 36 scans. The specimens were placed on a wooden stand covered by absorbers. The top of the radar was positioned at 96 cm above the ground to aim at the middle of
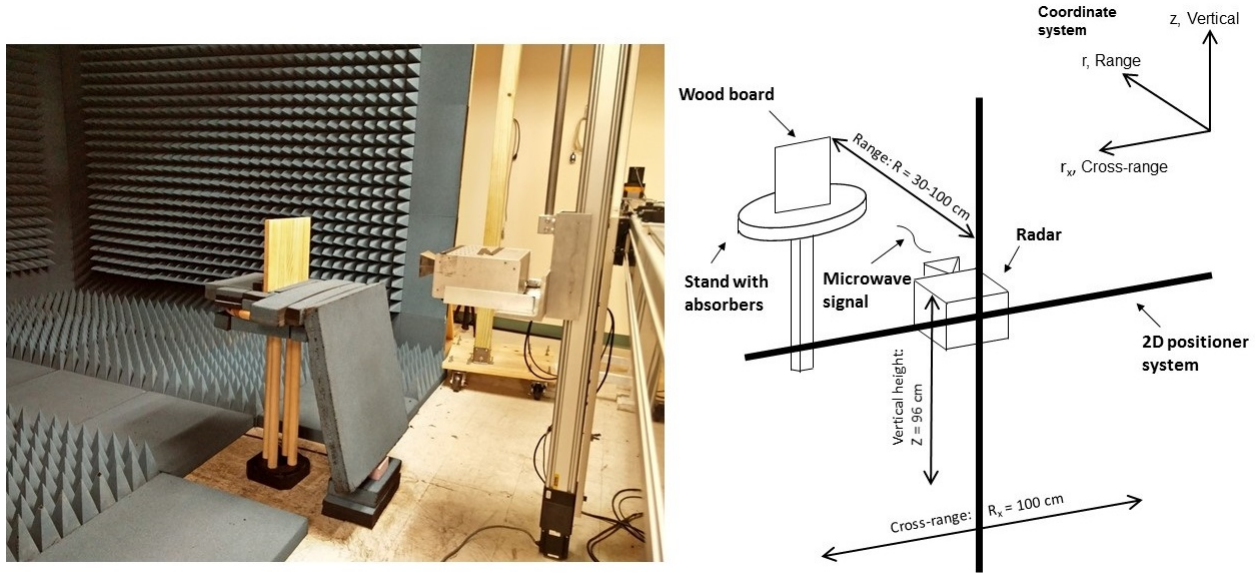
Figure 2. Setup and schematic for CWIR scan of wood board.

the specimen. Fig. 2 shows an example with a schematic of how one of the scans for the wood board was set up. Range axis is defined by r, cross-range axis is defined by r_x, and the vertical axis is defined by z. The incident angle of emitted EM waves on the specimens was 90°. The scans were conducted within a cross-range of 30 cm ($R_x = 30$ cm) for the wood and steel bars and within a cross-range of 100 cm ($R_x = 100$ cm) for the wood board and steel plate. The specimens were placed at the center of these cross-ranges. Since a stepping algorithm was used in the data collection of the radar system, the radar emitted EM waves and received the return through a periodic time cycle. The stepping interval was 0.3125 cm for both cross-ranges.

Figure 3. Specimens from left to right: steel plate, steel bar, wood bar, wood board.

4

4. RESULTS AND ANALYSIS OF SAR IMAGES

SAR images yielded matrices of data whose elements represent the SAR amplitude, indicating the specimen's interaction with EM waves. The amplitudes of each are converted into a colormap plot showing a two-dimensional planar view with range along the vertical axis and cross-range along the horizontal axis. Examples of the SAR images at range 30 cm ($R = 30$ cm) are shown in Fig. 4. The SAR images for the steel plate and the wood bar are placed on their respective higher and lower color scales to better visualize the differences in the SAR amplitudes. To interpret and characterize SAR images, properties such as maximum amplitude, cross-range amplitude slices, and total SAR amplitude were examined in this research. Studying these properties provides insights into the attenuation of the EM response with range, material property, and specimen size.
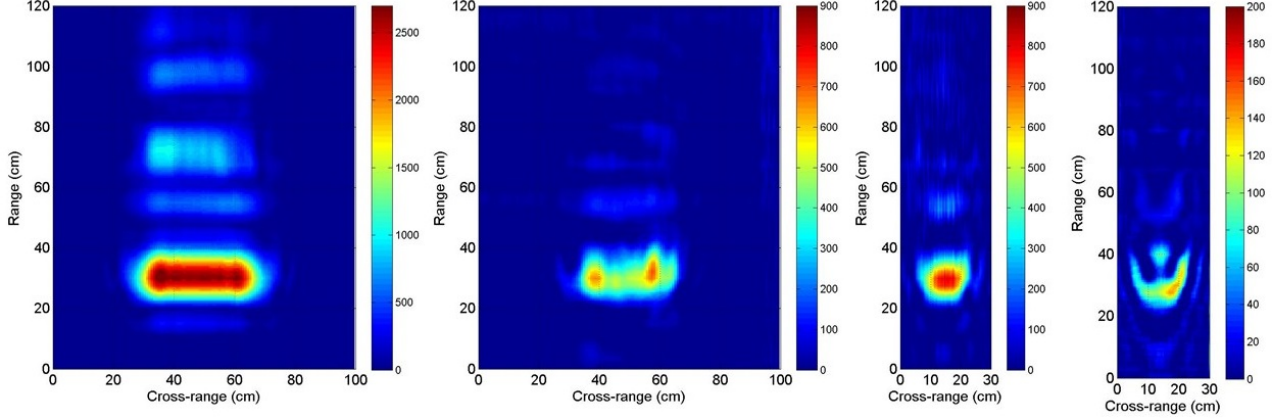

Figure 4. SAR image of specimens at range 30 cm from left to right: steel plate, wood board, steel bar, wood bar.

4.1 Maximum amplitude

Maximum amplitude with respect to range was first investigated in each SAR image. Maximum amplitude indicates the highest intensity of specular returns as collected by the imaging radar system. As the distance between the specimen and the radar increased, radar signals would naturally attenuate in greater amounts because of the longer distance of travel, causing specular returns to be weaker. For both steel specimens, this attenuation of radar signals and subsequent lowering of maximum amplitude was plotted against range in Fig. 5 and modeled by Eq. (5) for the steel plate and by Eq. (6) for the steel bar.

$$I_{max}(r) = \left(1.265 \times 10^4\right) r^{-0.2543} - 2,414 \tag{5}$$

$$I_{max}(r) = (4,800)r^{-0.5465} - 94.36 \tag{6}$$

I_{max} represents the maximum amplitude in the SAR image, and r is the range distance in centimeters. As expected, an increase in range reduces the amount of specular returns captured by the radar. (Note: Ideally, maximum amplitudes should match the range at which the scan was conducted; however, inaccurate placement of the specimen, especially with the smaller bars, could occur.)

On the other hand, the wood specimen did not exhibit the same descending progression in maximum amplitudes. As seen from Fig. 6, the maximum amplitude interchanged between increasing and decreasing trends as range was raised from 30 cm to 100 cm; therefore, an appropriate modeling curve was not found for the wood. Unlike the conducting characteristics of the steel plate and bar, the wood specimens were dielectric materials. In the steel specimen, signals were simply bounced off the face through specular return and collected by the radar system. However, additional mechanisms of signal interaction between the EM waves and the wood specimens occurred. Along with specular return of signals from the face of the wood specimen, their dielectric properties caused multiple reflections through penetration of its thickness. In addition, signals reflected through and around the edges, complicating the response even further. These edge reflections were coupled by the effects from the edges of the specimens. In total, three mechanisms determined the SAR image amplitudes of the wood
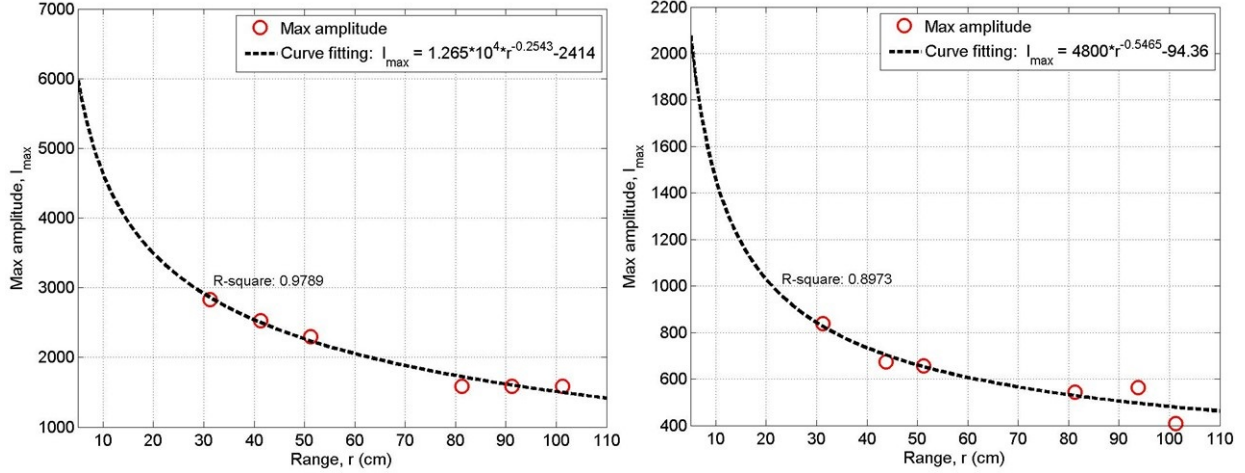
Figure 5. Maximum amplitude curve fitting of a steel plate (left) and a steel bar (right).

specimens: specular return off the front face, multiple reflections within their thicknesses, and edge reflection through and around their edges. As a result, maximum amplitudes did not follow any particular pattern with range.
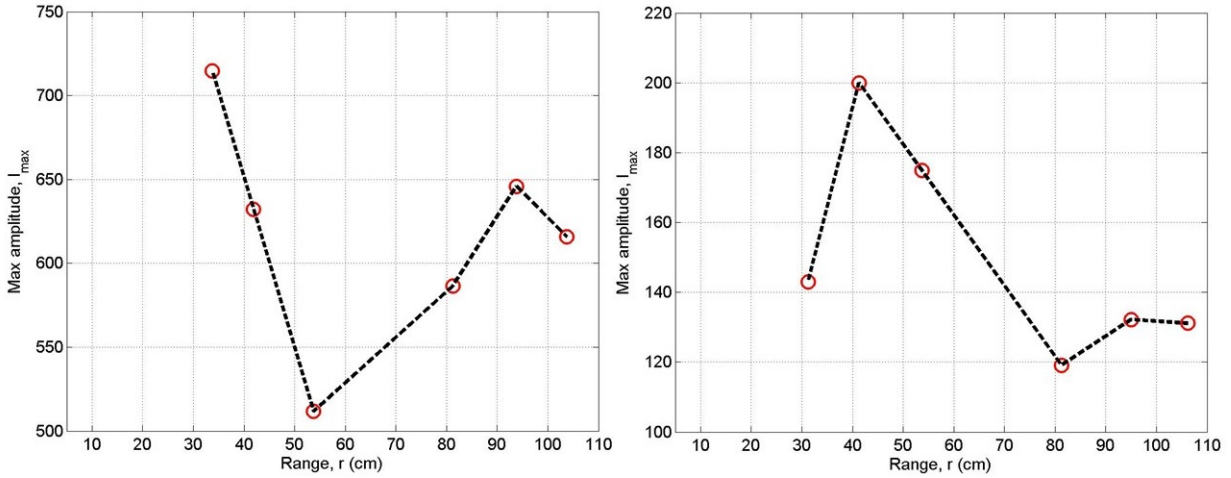

Figure 6. Maximum amplitude variation against range for a wood board (left) and a wood bar (right).

By considering all these maximum amplitude curves together, the steel plate was easily distinguishable from the three other specimens. With a larger surface area and with electrically conducting material properties, the steel plate reflected a significant amount of EM waves which were collected by the radar system and interpreted as higher maximum amplitudes. Furthermore, the steel bar, due to its properties as a perfect electric conductor (PEC), yielded SAR amplitudes that were far greater than that of its wood counterpart, despite having the same size dimensions.

4.2 Cross-range amplitude slice

Recall that the SAR image matrix composed of elements that corresponded to amplitudes of intensity of specular returns, with the rows correlating to the cross-range direction and the columns correlating to the range direction. Cross-range amplitude slices were obtained by selecting an entire row of amplitude values at one range, or column of the SAR image matrix. Fig. 7 shows examples of these slices for each specimen at range 40 cm ($R = 40$ cm).

Examining these slices provided a criterion for differentiating sizes of the same material. The cross-range amplitude slices of the larger steel plate and wood board exhibited high amplitude maximums corresponding to

the edges of the specimen. For the wood board, this phenomenon could be explained by the multiple mechanisms described earlier that dictate the intensity of the specular returns and signal attenuation. On the other hand, the maximum amplitudes at the edges for the steel plate were assumed to be caused by EM waves creeping around its front surface and interacting with its sides to produce greater amplitudes at these two ends. Amplitudes of the steel plate and wood board between these two points were lower than these maximums but still significantly greater than any amplitude from their smaller counterparts. On the contrary, the effects at the edges of the bars were not easily seen since their widths were considerably smaller than their large counterparts. Hence, their cross-range amplitudes appeared as a hill with the maximum amplitude occurring approximately at the center of the cross-range slice where the specimen would be located.
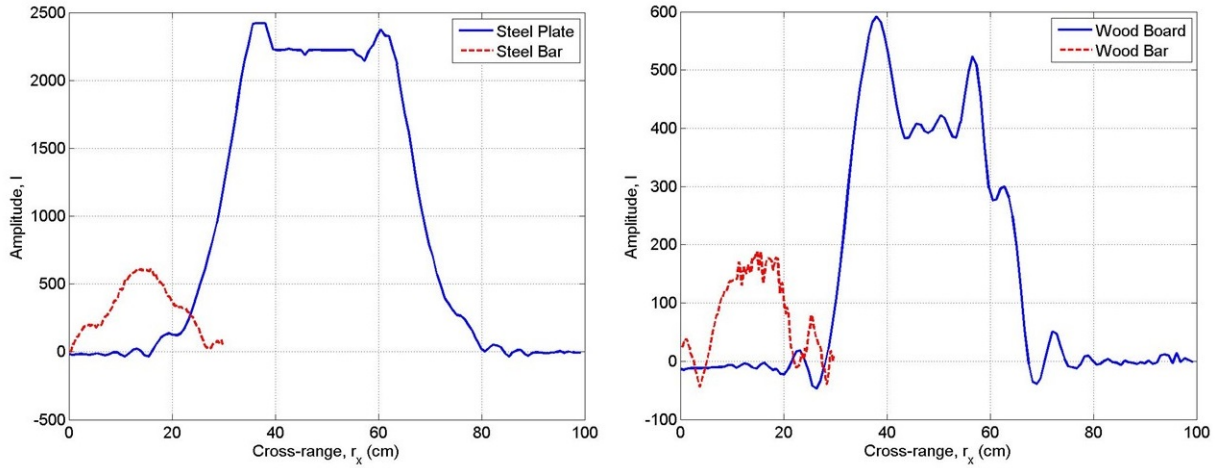

Figure 7. Cross-range slice at R = 40 cm for steel specimens (left) and wood specimens (right).

As the steel plate and the wood board were placed further away from the radar, the effects of amplified specular return at the edges converged closer to each other in cross-range distance. As seen in Fig. 8 for the steel plate, the width between the two maximum amplitudes shortened with an increase in range. This trend was plotted in Fig. 9 and modeled by Eq. (7) and Eq. (8).
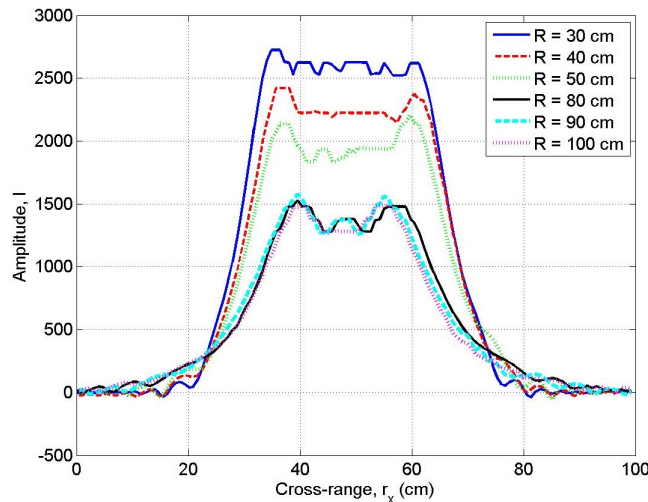

Figure 8. Cross-range slice at R = 30, 40, 50, 80, 90, 100 cm for a steel plate.

7

$$W_{steel}(r) = \left(-3.599 \times 10^{-4}\right) r^2 - 0.1335r + 30.74 \tag{7}$$

$$W_{wood}(r) = \left(-8.261 \times 10^{-7}\right) r^{3.505} + 18.99 \tag{8}$$

W_{steel} and W_{wood} represent the distance between the two maximum amplitudes of the steel plate and wood board in centimeters, respectively, and r is the range in centimeters. To explain this trend, one should consider how the radar would "see" the specimen as it moved further away. Just as how a large object would appear much smaller to an observer with a long distance between them, the same would happen to the steel plate and wood board in the vision of the radar. Eventually, the effects of specular return and signal attenuation at the edges and the center of the steel plate and wood board would converge and, similar to those of their smaller counterparts, the resulting cross-range amplitude slices would appear as a hill with a maximum at the center.
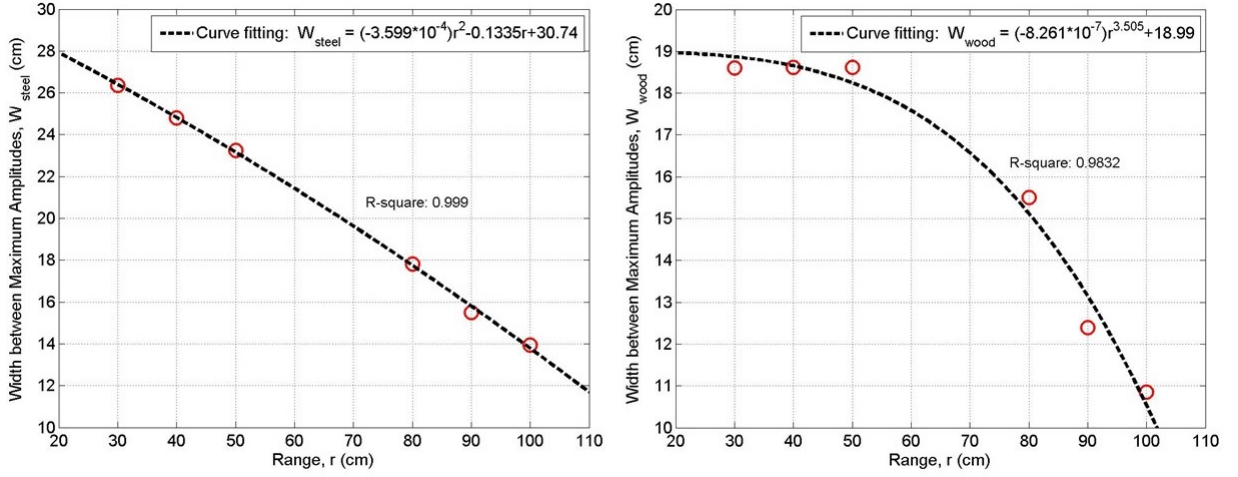

Figure 9. Decrease in width between maximum amplitudes against range for steel plate (left) and wood board (right).

Since cross-range amplitude slices were obtained at various ranges for the steel plate and steel bar, three-dimensional (3D) models of amplitudes as they varied with range and cross-range were developed. Again, because of the complication due to multiple mechanisms of interaction with EM waves and the wood board and bar, the slices of these specimen were not able to be modeled.

$$I_{sp}(r, r_x) = 811.10 - 220.40r_x + 11.57r_x^2 - 0.17r_x^3 + (7.99 \times 10^{-4})r_x^4 + (-8.74 \times 10^{-7})r_x^5 \tag{9}$$
$$+ r[-2.78 + 0.86r_x - 0.043r_x^2 + (5.67 \times 10^{-4})r_x^3 + (-2.20 \times 10^{-6})r_x^4]$$

$$I_{sb}(r, r_x) = 72.51 - 38.53r_x + 2.33r_x^2 - 0.034r_x^3 + (1.64 \times 10^{-4})r_x^4 + (-1.89 \times 10^{-7})r_x^5 \tag{10}$$
$$+ r[-1.36 + 0.27r_x - 0.014r_x^2 + (1.86 \times 10^{-4})r_x^3 + (-7.12 \times 10^{-7})r_x^4]$$

These models, represented by fifth-order polynomials of Eq. (9) for the steel plate and Eq. (10) for the steel bar, assumed the steel specimens to be positioned in the center of the cross range. In addition, the edge effects of the steel plate were ignored. The models along with the slices used for the fitting are shown in Fig. 10. The R-square value of the curve fitting was 0.9294 for the steel plate and 0.8872 for the steel bar. The models estimated amplitude values of scans conducted at ranges between 30 cm and 100 cm and at cross-range 100 cm for the steel plate and 30 cm for the steel bar.
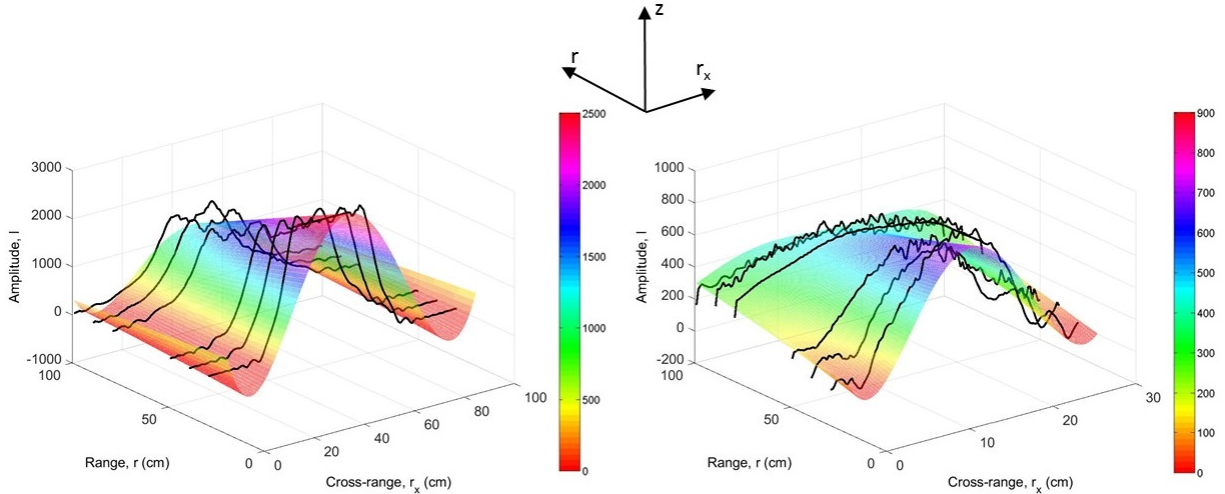
Figure 10. 3D modeling of amplitudes of steel plate (left) and steel bar (right) with respect to range and cross-range.

Table 1. Largest percent difference of maximum amplitude and total SAR amplitude criteria.

	Range (cm)					
	30	**40**	**50**	**80**	**90**	**100**
Maximum Amplitude (%)	34.96	4.52	5.56	6.95	10.01	34.75
Total SAR Amplitude (%)	25.47	23.13	11.32	16.30	36.40	91.76

4.3 Total SAR amplitude

Total SAR amplitude, an accumulation of the amplitudes of the SAR image matrix, provides an additional perspective to analyze the SAR images. For the steel plate, the steel bar, and the wood board, total SAR amplitude yielded the same results as the other criteria. However, it was more capable than the maximum amplitude and cross-range amplitude slices at differentiating the wood bar as it was scanned at various orientations (rotated about its vertical 90° and 180°). Fig. 11 shows an example of how the wood bar's SAR image changed at range 30 cm with its rotation about the vertical axis.

The SAR image of the bar when rotated 90° was more prominent and stronger than those of the other two orientations. At other ranges, similar differences were found in the rest of the SAR images, with no one orientation consistently dominating the other two in terms of amplitude. Apart from range 30 cm, there was little difference in maximum amplitude among the three orientations. However, using the total SAR amplitude criterion revealed a greater disparity for additional ranges. This comparison can be seen in Fig. 12. The largest percent difference at each range for both criteria are compared in Table. 1. The percent difference of the maximum amplitude criterion was minimal in most cases. Total SAR amplitude was able to outperform maximum amplitude in demonstrating the differences of the wood bar among the three orientations.

The differences among the orientations were related to the grains of the wood bar. Fig. 11 shows the different grain orientations of the wood bar. Radar signals were able to penetrate the wood as a low-loss dielectric material. The bar's grains interacted with the radar signals differently with each amount of rotation, resulting in the varying increases and decreases in total SAR amplitude. If the wood bar were uniform in composition, the amplitudes among the three orientations would be expected to remain similar to one another at each range. This finding demonstrated the radar's performance in identifying the subsurface properties of a dielectric material like wood.

5. SUMMARY

Research findings for developing criteria to differentiate size and material properties for a steel plate, a steel bar, a wood board, and a wood bar within ranges between 30 and 100 cm and at cross-ranges of 30 cm and 100 cm are summarized in the following.
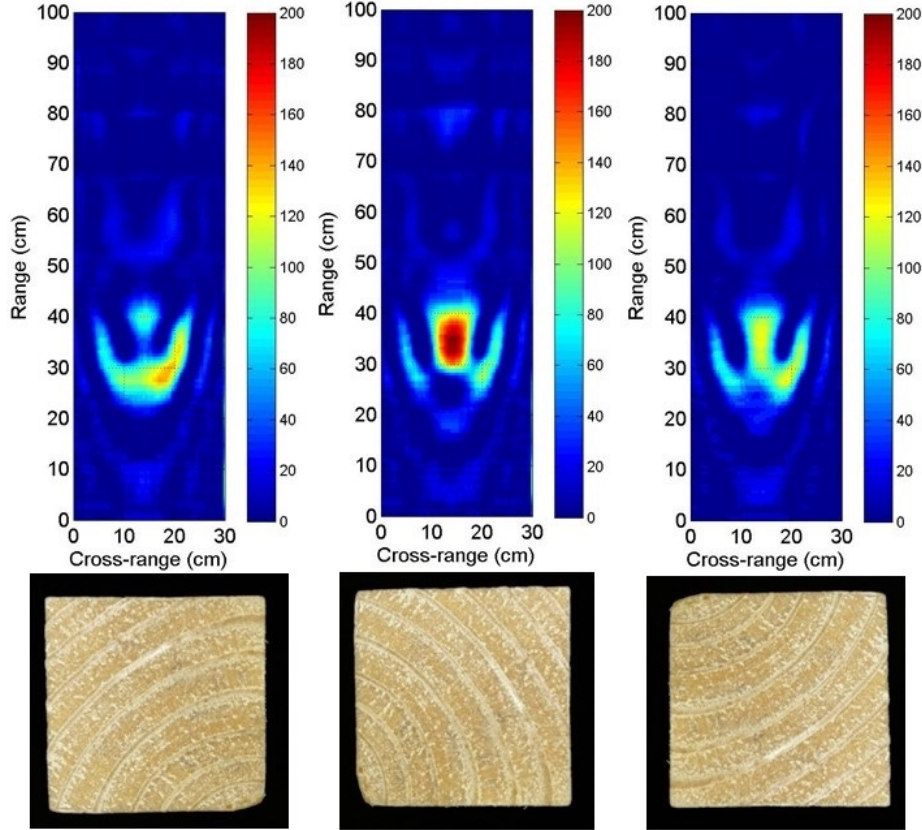
9

Figure 11. SAR image of wood bar in original orientation (left), when rotated 90° (middle), and when rotated 180° (right).
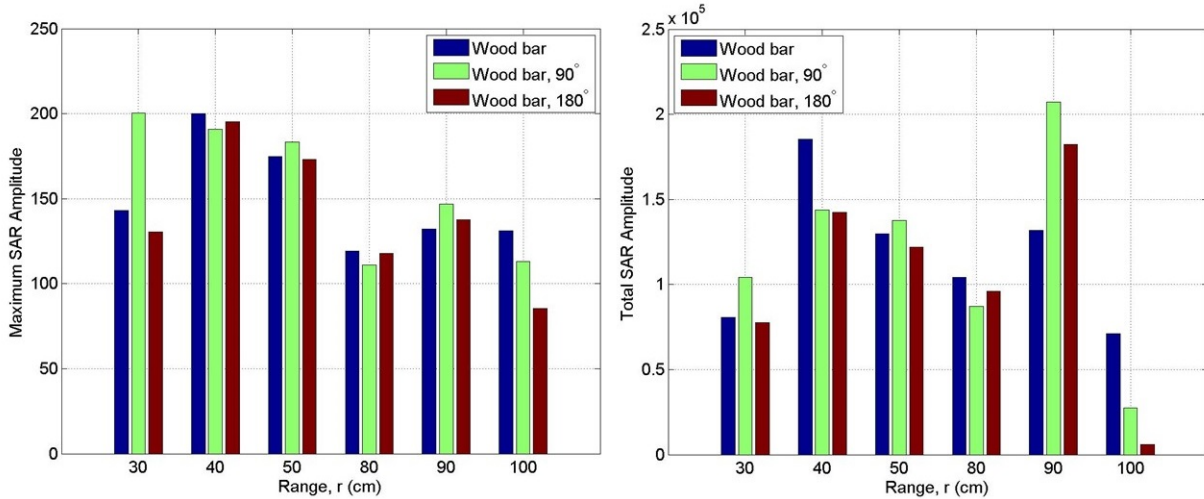

Figure 12. Comparison of maximum amplitude (left) with total SAR amplitude (right) for SAR images of wood bar.

- Maximum SAR amplitude – The steel plate exhibited the highest maximum amplitude at each range because of its larger size and EM property (perfect electric conductor). The steel bar yielded greater amplitudes than its wood counterpart of the same size. Decrease of amplitude due to attenuation of radar signals with respect to range was modeled by Eq. (5) for the steel plate and Eq. (6) for the steel bar. Decrease of amplitude with respect to range for the wood specimens were complicated by other mechanisms of EM wave scattering inside the wood board and the wood bar.

- Cross-range amplitude slices – It was found that cross-range amplitude slices can differentiate materials of two different sizes. The larger steel plate and wood board had slices characterized by two values of maximum amplitudes corresponding to the edges of the specimen. The decrease in width between these two maximum amplitudes with respect to range were modeled by Eq. (7) for the steel plate and Eq. (8) for the wood board. Slices of both steel bar and wood bar were distinguished by one maximum amplitude value occurring approximately at the center of the cross-range. The edge effects on the attenuation of radar signals were not seen because of the smaller cross-sectional width of the specimen in the orientation of which they were scanned. Lastly, these cross-range amplitude slices at the six ranges were used to model the amplitude values as they changed in both range and cross-range directions. These 3D models were represented by Eq. (9) for the steel plate and Eq. (10) for the steel bar.

- Total SAR amplitude – Total SAR amplitude differentiated a wood bar at different orientations (original position, rotated by 90°, and rotated by 180°). Maximum amplitude was not used because of the similarities among the values at certain ranges. Total SAR amplitude was able to better reveal how the grains of the wood bar affect the scattering of radar signals. The subsurface sensing capabilities of the radar system were thus demonstrated.

6. CONCLUSION

SAR imaging is a promising technology that can improve the resolution of EM methods for the surface and subsurface sensing of construction materials in a remote sensing approach. An understanding of how these materials are portrayed by SAR imaging must be obtained before this technology can be utilized to its full potential. The experimental work reported in this paper contributes to the series of comprehensive laboratory tests that are required to thoroughly understand the interaction of radar signals with perfect electric conductors (PEC) (e.g. steel) and dielectric materials (e.g. wood).

7. ACKNOWLEDGMENT

8. DISCLAIMER

The views, opinions, findings and conclusions reflected in this presentation are the responsibility of the authors only and do not represent the official policy or position of the DOE, DOT/OST-R, or any State or other entity.

REFERENCES

[1] American Society of Civil Engineers (ASCE), "2015 report card for New York's infrastructure." Online (2015).
[2] American Society of Civil Engineers (ASCE), "2015 report card for Virginia's infrastructure." Online (2015).
[3] American Society of Civil Engineers (ASCE), "2015 report card for Arizona's infrastructure." Online (2015).
[4] American Society of Civil Engineers (ASCE), "2015 report card: A call to action for Iowa's infrastructure." Online (2015).
[5] Wiggenhauser, H., Helmerich, R., Taffe, A., Kraise, M., Kind, T., Lai, W.-L., Scheel, H., Wilsch, G., and Niederleithinger, E., "Nondestructive testing in civil engineering," Ullmann's Encyclopedia of Industrial Chemistry , 541–573 (2012).
[6] Verma, S. K., Bhadauria, S. S., and Akhtar, S., "Review of nondestructive testing methods for condition monitoring of concrete structures," Journal of Construction Engineering (2013).
[7] Annan, A. P., "GPR–history, trends, and future developments," Subsurface Sensing Technologies and Applications 3(4), 253–270 (2002).

[8] Annan, A., "Chapter 1 - electromagnetic principles of ground penetrating radar," in [Ground Penetrating Radar Theory and Applications], Jol, H. M., ed., 1 – 40, Elsevier, Amsterdam (2009).

[9] Colla, C., Krause, M., Maierhofer, C., Höhberger, H., and Sommer, H., "Combination of NDT techniques for site investigation of non-ballasted railway tracks," NDT & E International 35(2), 95 – 105 (2002).

[10] Saarenketo, T., "Chapter 13 - NDT transportation," in [Ground Penetrating Radar Theory and Applications], Jol, H. M., ed., 393 – 444, Elsevier, Amsterdam (2009).

[11] Kharkovsky, S., Case, J. T., Ghasr, M. T., Zoughi, R., Bae, S. W., and Belarbi, A., "Application of microwave 3D SAR imaging technique for evaluation of corrosion in steel rebars embedded in cement-based structures," AIP Conference Proceedings 1430(1) (2012).

[12] Lai, C.-P., Ren, Y.-J., and Yu, T. Y., "Scanning array radar system for bridge subsurface imaging," Proc. SPIE 8347, 834713 (2013).

[13] Yu, T., "Distant damage-assessment method for multilayer composite systems using electromagnetic waves," Journal of Engineering Mechanics (ASCE) 137(8), 547–560 (2011).

[14] Yu, T., Su, C.-F., Lai, C.-P., and Wu, H. F., "Wideband subsurface radar for bridge structural health monitoring and nondestructive evaluation," Proc. SPIE 8694, 86940I (2013).

[15] Cutrona, L. J., "Chapter 21 - synthetic aperture radar," in [Radar Handbook], Skolnik, M. I., ed., 21.1 – 21.23, McGraw-Hill (1990).

[16] Yegulalp, A., "Fast backprojection algorithm for synthetic aperture radar," in [Proceedings of the 1999 IEEE Radar Conference], 60–65 (1999).